International Journal of Nanomedicine

Dovepress
Taylor & Francis Group

Open Access Full Text Article

ORIGINAL RESEARCH

iRGD-Targeted Biosynthetic Nanobubbles for Ultrasound Molecular Imaging of Osteosarcoma

Tingting Liu[1–3], Xiaoxin Liang[4], Wei Liu[5], Shuai Yang[6], Tao Cui[7], Fei Yan[3], Zhenzhou Li[1,2]

[1]Department of Ultrasound, The second People's Hospital of Shenzhen, The First Affiliated Hospital of Shenzhen University, Shenzhen, 518061, People's Republic of China; [2]Graduate School, Guangxi University of Chinese Medicine, Nanning, 530200, People's Republic of China; [3]CAS Key Laboratory of Quantitative Engineering Biology, Shenzhen Institute of Synthetic Biology, Shenzhen Institutes of Advanced Technology, Chinese Academy of Sciences, Shenzhen, 518055, People's Republic of China; [4]Department of Ultrasound, Sun Yat-Sen University Cancer Center, Guangzhou, 510060, People's Republic of China; [5]School of Life Sciences, Sun Yat-Sen University, Guangzhou, 510275, People's Republic of China; [6]Department of Clinical and Research, Shenzhen Mindray Bio-Medical Electronics Co, Ltd, Shenzhen, 518055, People's Republic of China; [7]Medical Imaging center, Shenzhen Yunshan Yunli Hospital, Shenzhen, 518055, People's Republic of China

Correspondence: Fei Yan; Zhenzhou Li, Email fei.yan@siat.ac.cn; lizhenzhou2004@126.com

Purpose: Osteosarcoma is the most common primary malignant tumor of the bone. However, there is a lack of effective means for early diagnosis due to the heterogeneity of tumors and the complexity of tumor microenvironment. αvβ3 integrin, a crucial role in the growth and spread of tumors, is not only an effective biomarker for cancer angiogenesis, but also highly expressed in many tumor cells. Here, we selected it as the imaging target and fabricated iRGD-sGVs acoustic probe for the early-stage diagnosis of osteosarcoma.

Materials and Methods: Biological nanoscale gas vesicles (sGVs) were extracted from *Serratia 39006*. Their morphology was analyzed with phase contrast and transmission electron microscopes. Particle size and zeta potential were measured by a Zetasizer. iRGD-targeted molecular probes (iRGD-sGVs) were prepared by coupling iRGD to sGVs via Mal-PEG2000-NHS. Targeting efficiency of iRGD-sGVs was evaluated using flow cytometry and confocal microscopy on endothelial and K7M2 osteosarcoma cells. In vivo contrast-enhanced ultrasound imaging of iRGD-sGVs was performed in osteosarcoma-bearing mice, and the expression of $a_v\beta_3$ in osteosarcoma was detected through immunofluorescence staining assay. Biocompatibility of sGVs was assessed by hemolysis tests, CCK8 cytotoxicity assays, blood biochemical tests, and HE staining.

Results: sGVs from *Serratia*.39006 have smaller particle size (about 160 nm). Our in vitro and in vivo experiments showed the specifically binding ability of iRGD-sGVs to both vascular endothelial cells and tumor cells, producing the stronger and longer acoustic signals in tumors in comparison with the control probe. Immunofluorescence staining results indicated iRGD-sGVs were co-localized with highly expressed αvβ3 in tumor vasculature and osteosarcoma cells. Biocompatibility analysis showed no significant cytotoxicity of iRGD-sGVs to mice.

Conclusion: Our study provides a new strategy for early diagnosis of osteosarcoma.

Keywords: ultrasound molecular imaging, ultrasound contrast agents, gas vesicles, internalizing RGD, tumor imaging

Introduction

Osteosarcoma, characterized by a high degree of malignancy, strong invasiveness, rapid disease progression, and extremely high mortality rate, is the most common primary malignant tumor of the bone. It accounts for approximately 20% of all primary bone tumors and is considered as a serious threat to the human health globally.[1,2] In recent years, numerous new medical imaging technologies bring great advance for precise diagnosis and treatment of osteosarcoma.[3–6] However, the early diagnosis of osteosarcoma still faces big challenges due to the heterogeneity of tumors and the complexity of the microenvironment.[7,8] Molecular imaging is an innovative imaging technology that combines biomedical imaging and molecular biological detection, enabling the visualization, characterization, and measurement of biological processes at the molecular and cellular levels in a noninvasive way. By employing some specific imaging

Received: 4 October 2024
Accepted: 4 January 2025
Published: 20 January 2025

Graphical Abstract

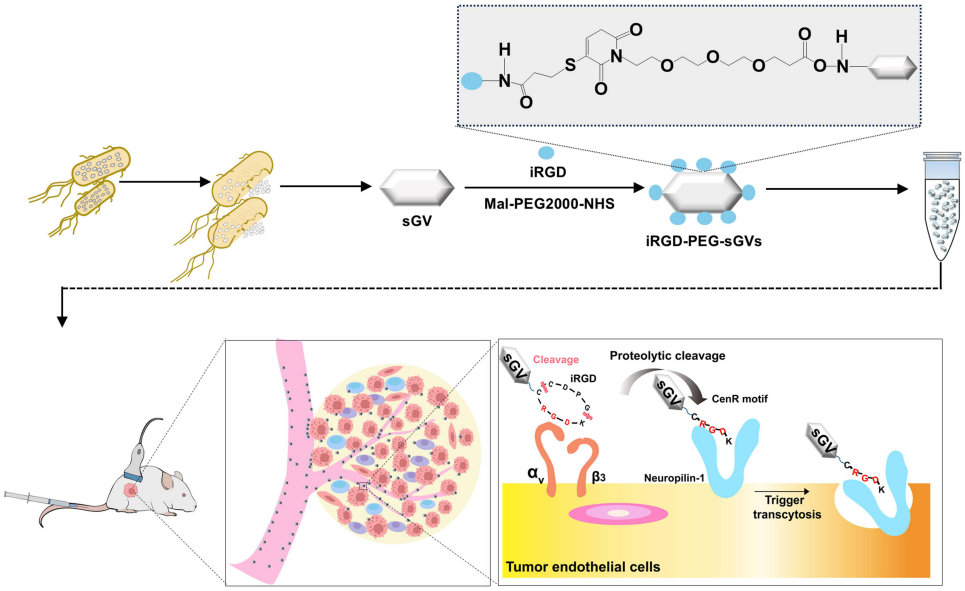

probes or tracers, it can reveal the physiological activities or expression status of specific molecules within tumors, with great advantages over conventional imaging modalities that primarily images differences in the structure of tumors.[9,10]

To date, researchers have developed numerous imaging probes from various medical imaging modalities, including positron emission tomography (PET), optical imaging, photoacoustic (PA), magnetic resonance imaging (MRI), and ultrasound (US). Each imaging modality has its relative advantages and limitations. In comparison, ultrasound molecular imaging has more advantages over its disadvantages. Ultrasound is noninvasive, relatively inexpensive, portable, and has an excellent temporal resolution. Also, it is considered one of the least harmful imaging techniques. By using of molecularly-targeted bubbles, ultrasound molecular imaging can visualize molecular and genetic alterations of diseased cells, making it possible to achieve early-stage diagnosis of tumors.[11] Nowadays, numerous ultrasound molecular imaging probes have been constructed through coating microbubbles with various targeting ligands (including antibodies, peptides, nucleic acids, and small molecules, etc.), aiming to provide specific interactions with targets overexpressed in the diseased tissues, thereby offering strong contrast signals for early screening, diagnosis, and treatment of cancer.[12–15] However, most of them utilized chemically synthesized microbubbles contrast agents which have many defects in imaging of tumor. For example, the particle size of microbubbles is typically 1–5 μm, making it difficult pass through tumor blood vessels and target to tumor cells. In recent years, biologically synthesized nano-scale gas vesicles (GVs) have gradually shown their advantages as good contrast agents. Compared with chemically synthesized bubbles, the biosynthesized GVs have some obvious advantages. Firstly, GVs can be encoded by gvp genes, which makes them easier to genetical manipulation. Secondly, GVs are formed in the bacterial cells, endowing them with better biocompatibility. More importantly, the production process of GVs is lower cost than chemically synthesized nanobubbles, facilitating GVs for clinical translation. Our previous studies revealed ligand-modified gas vesicles (hGVs, with a particle size of 200 nm) extracted from *Halobacterium sp. NRC-1* can be used as molecular probes for imaging of tumor cells.[16,17] But there is still a lack of sufficient blood circulation time.[18] To address this issue, we synthesized a new biologically nano-scale gas vesicle from *Serratia*.39006 (sGVs), with a particle size of approximately 160 nm, showing the potential to improve blood circulation time.[19]

To enhance the molecular imaging effect, in this study, we selected iRGD peptide and conjugated them onto the sGVs from *Serratia*.39006 to construct the tumor-targeted acoustic probes. iRGD is a cyclic nonapeptide (CRGDKGPDC) which can bind to $\alpha_v\beta_3$ integrin with high affinity and specificity. $\alpha_v\beta_3$ integrin, a crucial role in

the growth and metastasis of tumors, is not only an effective biomarker for cancer angiogenesis, but also highly expressed in many tumor cells.[20] Numerous literatures have proved that iRGD can effectively improve the permeability of nanoprobes, contrast agents and nanodrugs into tumors.[21,22] In this study, we report the iRGD-modified acoustic nanoprobes, based on biologically synthesized sGVs from *Serratia*, and explore their potential in the precise diagnosis of osteosarcoma.

Materials and Methods

Materials

Fluorescein isothiocyanate (FITC)-labeled iRGD (iRGD-FITC, with an amino acid sequence: CRGDKGPDC, produced by Shanghai Apeptide Co., Ltd) and FITC-labeled control peptide (Con-FITC, with an amino acid sequence: CNGRKGTRC) were synthesized by GL Biochem (Shanghai) Ltd. The *Serratia.39006* strain used in this study was purchased from the American Type Culture Collection (ATCC). SoluLyse bacterial protein extraction reagent (Tris Buffer, pH 7.4, Item Number: L200500, Brand: Galantis) was purchased from Shenzhen Chemical Test Technology Co., LTD. Lysozyme (Item number: L8120-50g, Brand: Soleibao) and DNase I (CAS Number: 9003–98-9, Brand: GLPBIO) were purchased from Beyotime Institute of Biotechnology. Cell counting kit-8 (CCK8, CAS Number: BS350B, Brand: biosharp) was purchased from Guangzhou Saiguo Biotechnology Co., LTD. LB medium (no sugar) and LB agar (without sugar, Item number: 28324) from HuanKai Microbial were used for *Serratia* cultivation. Maleimide-polyethylene glycol 2000-active ester (Mal-PEG2000-NHS, CAS Number: R-1106-2K, Brand: Ruixibio) was purchased from Risi Bio. Dialysis bags (CAS Number: YA-1068, Brand: Solarbio) were purchased from Shenzhen Shangxing Technology Co., LTD. Calcein-AM/PI Double Stain Kit (Cat:40747ES80, Brand: Yeasen) was purchased from Shenzhen AOKE Biotechnology Co., LTD. The K7M2 cell line and murine bEnd.3 endothelial cells were purchased from the American Type Culture Collection. BALB/c mice (approximately 20 g body weight) were obtained from the Guangdong Medical Laboratory Animal Center.

Isolation of Gas Vesicles (GVs)

Briefly, *Serratia.39006* was cultured in LB medium at 30°C in an orbital shaker with 200 rpm shaking for 72 h. Cells were collected and subsequently centrifuged at 800 g for 2 h to remove the intermediate liquid layer. The collected bacterial samples were subsequently lysed with SoluLyse Bacterial Protein Extraction Reagent and lysozyme, and gently stirred at room temperature for 2 h, followed by the addition of DNase I and incubation for another 2 h. Then, the upper floating bacteria were collected by centrifugation and repeated 3–5 times. Finally, the purified sGVs were stored in PBS at 4°C. The concentration of sGVs was determined at a wavelength of 500 nm using a microplate reader (Multiskan GO, Thermo Scientific, Waltham, MA, United States). Meanwhile, sGVs and their bacterial samples were observed by phase-contrast microscopy (PCM, Olympus IX83 inverted microscope, Tokyo, Japan) and transmission electron microscopy (TEM, Hitachi H-7500, Hitachi Limited, Tokyo, Japan). The bacterial cells and sGVs were diluted to appropriate concentrations and dropped onto a coverslip coating with 1% agar. Imaging of the cells were carried out by using a phase-contrast microscope (IX83-SIM) under a ×100 oil objective. Furthermore, they were diluted and carefully placed upon copper mesh, negatively stained with 2% phosphotungstic acid, and dried at room temperature. TEM was used to observe the morphology of GVs.

Preparation and Characterization of iRGD-sGVs and Con-sGVs

Firstly, 10 mg Mal-PEG2000-NHS was reacted with 1mL sGVs (OD_{500} 3.0) at 37°C for 4 h. Then, free Mal-PEG2000-NHS was removed by dialysis (Solarbio MWCO: 1000 kDa) with PBS solution for 10 h. Using the Michael reaction, the fluorescein-labeled targeted nanobubbles (FITC-iRGD-sGVs) were fabricated through incubating FITC-iRGD with MAL-PEG-GVs at 4°C overnight. FITC-Con-sGVs were prepared by using the same method. The fluorescence intensity was measured by a microplate reader to confirm the successful conjugation. Particle size and zeta potential of sGVs were measured using a Zetasizer analyzer (Zetasizer Nano S90, Malvern, Worcestershire, UK). All samples were diluted to appropriate concentrations at room temperature.

In vitro Imaging and Characterization of sGVs

An in vitro imaging phantom was prepared using a custom-made 1.5% (w/v) agarose mold. Subsequently, different concentrations of iRGD-sGVs or Con-sGVs (OD_{500} = 1.0, 1.5, 2.0, 2.5) were added to these agar wells. Imaging was performed using an ultrasound diagnostic device (Mindray Resona 9T, Mindray, Shenzhen, China) equipped with an L11-3U linear array transducer. The ultrasonic probe was placed directly on the side of the agarose. The parameters were kept as follows: acoustic power: 8.91%, mechanical index: 0.220, contrast gain 70 dB. The imaging performance of sGVs and chemically synthesized phospholipid nanobubbles were also evaluated at different MI from 0.03 to 0.41. Furthermore, the stability of iRGD-sGVs was investigated by measuring the particle size and zeta potential at 0, 2, 4, 6, 8, 10, 15 and 20 days using the Zetasizer analyzer.

Cell Culture

Murine bEnd.3 endothelial cells and K7M2 mouse osteosarcoma cells were cultured in Dulbecco's modified Eagle's medium containing 10% fetal calf serum (Gibco), and 1% penicillin–streptomycin solution, and kept in a humidified atmosphere containing 5% CO_2 at 37°C.

In vitro Cell Targeting Studies

bEnd.3 cells at 80% cell density were selected for the in vitro cell targeting studies. Briefly, 1×10^5 cells were resuspended in 300 μL PBS and divided into 1.5 mL EP tubes. A 5 μg FITC-iRGD and FITC-Con peptides were added to the tubes to incubate on ice for 30 min. For the cell competition experiment, 5 μg free iRGD peptide was added to the cell suspension for about 1h on ice, then 5 μg FITC-iRGD was added for 30 min. All samples were washed 2–3 times with sterile PBS. K7M2 cells were performed in the same manner.

For in vitro binding of iRGD-sGVs to tumor cells, 1×10^4 bEnd.3 cells were seeded in 24-well plates and placed in a cell incubator overnight. The cell adhesion assay was performed. In brief, the cells were fixed with 4% paraformaldehyde. A 100 μL FITC-iRGD-sGVs or FITC-Con-sGVs (OD_{500} at 1.5) was added to each well, respectively. All samples were incubated in dark at room temperature for 10 min and then washed three times with cold PBS for 5 min each time. After that, these cells were stained with DAPI and the cells were observed under a confocal microscope. The unlabeled free iRGD peptides were used for pre-incubation with cells for 30 min at room temperature, and then FITC-iRGD-sGVs was added for competitive inhibition experiments. The K7M2 osteosarcoma cells were performed in the same manner. Images were recorded using confocal microscope (A1R, Nikon, Japan) and quantified using Image J software.

Animal Model

All animal experiments were carried out in compliance with the relevant laws and institutional guidelines for the care and use of laboratory animals. Protocols were approved by the Committee on the Ethics of Animal Experiments of Shenzhen Institutes of Advanced Technology, Chinese Academy of Science (protocol NO: SIAT-IACUC-231114-HCS-YF-A2377; date of approval: 14 November September 2023). All imaging procedures were performed under isoflurane inhalation anesthesia, and all efforts were made to minimize suffering. The K7M2 mouse osteosarcoma cells in 100 μL PBS were injected into the right back BALB/c mice. Tumor-bearing mice were used for ultrasound imaging when they had developed palpable tumors (about 5–10 mm in diameter) after inoculation.

In vivo Ultrasound Imaging Assay

During ultrasound imaging, mice BALB/c were anesthetized with oxygen containing 1% isoflurane at 2 L/min on a heating pad. iRGD-sGVs and Con-sGVs (150 μL, OD_{500} at 3.2) were injected into mice (n = 5) through the tail vein in random order to minimize bias, and ultrasound imaging was performed using a Mindray Resona 9T equipped with a line array transducer. All parameters (acoustic power: 8.91%, mechanical index: 0.220, contrast gain: 70 dB) were kept constant during imaging procedure. Images were acquired continuously for 15 min. To minimize any deviations from two injections in the same mouse, injections were separated by at least 30 min. After manually defining the region of interest

(ROI), the average acoustic signal intensity of the ROI per frame was measured using ImageJ to quantify the contrast signals.

Histological Examination

All animals were euthanized immediately after ultrasound imaging, and tumor tissues were dissected for immunohistochemical assay. Tumor sections with 6 μm thick were cut using a cryostatic microtome (CM 1950, Leica, Heidelberg, Germany) and stained with $\alpha_v\beta_3$ monoclonal antibody (CAS Number: ER1911-52, Hangzhou Huaan Biotechnology Co., Ltd). K7M2 osteosarcoma cells were stained directly with anti-mouse $\alpha_v\beta_3$ and blood vessels were stained with CD31 according to the product instructions. Tissue fluorescence was examined under an inverted fluorescence microscope (Wuhan Servicebio Technology Company, China).

Biosafety Testing

For the hemolysis assay, 1 mL fresh blood was taken from BALB/c mice and diluted with 2 mL of PBS. Red blood cells (RBCs) were isolated from serum by centrifugation (4500 rpm, 5 min). After washing five times, RBCs were then diluted with 10 mL PBS. The RBC suspension (250 μL) was incubated with 1 mL PBS (negative control), distilled water (positive control), and iRGD-sGVs at different concentrations (OD_{500} at 1.0, 1.5, 2.0, 2.5, 3.0) for 3 h at 37°C. After that, the supernatant was centrifuged at 600 g for 2 h, and the absorbance of the supernatant (200 μL) at 541 nm was measured using a microplate reader (Multiskan GO, Thermo Scientific, Waltham, MA, United States), then hemolysis rate was calculated.

For the cell cytotoxicity, the cytotoxicity of iRGD-sGVs was quantitatively analyzed by CCK-8 assay. Briefly, K7M2 and bEnd.3 cells were seeded in 96-well plates at a density of 1×10^4 cells per well and incubated for 24 h. iRGD-sGVs at OD_{500} = 0.5, 1.0, 1.5, 2.0, 2.5 or 3.0 were incubated at 37°C for 6 h. Subsequently, 10 μL CCK-8 solution was added and incubated with cells for 2–3 h. Finally, the cell viability was determined by the absorbance value at 450 nm. Calcein-AM and PI staining were also used to confirm the cell cytotoxicity. In brief, K7M2 cells and bEnd.3 cells were incubated with sGVs and stained by Calcein-AM and PI staining, followed by observation with confocal microscopy.

For in vivo biosafety, 12 healthy mice were systemically injected with PBS, iRGD-sGVs or Con-sGVs (100 μL, OD_{500} = 3.2). Blood samples were collected from the ophthalmic artery after 7 days to detect liver function (alanine aminotransferase (ALT), aspartate aminotransferase (AST)) and renal function (blood urea nitrogen (BUN), creatinine (CREA)). After that, major organs (heart, liver, spleen, lung and kidney) were removed and fixed with paraformaldehyde (4%, W/V) for H&E staining (Wuhan Servicebio Technology Company, China).

Statistical Analysis

Data were expressed as mean ± standard deviation, and independent *t* test was used to compare the two groups. Multiple group comparisons were used for one-way ANOVA followed by Bonferroni's multiple comparison test. GraphPad Prism software was used for graphics and statistical analysis. *P < 0.05 was considered significant. **** for P < 0.0001.

Results

Preparation and Characterization of iRGD-sGVs and Con-sGVs

The GVs used in this study were extracted from *Serratia*.39006, and the isolation and purification procedure of sGVs is shown in Figure 1A. About 8 mL of OD_{500} 3.2 sGVs can be obtained for 1L of bacteria culture. After obtaining the sGVs, the targeted sGVs (iRGD-sGVs) were prepared using the Michael reaction, as shown in Figure 1B. Most of these bacteria were filled with sGVs, and sGVs could be visualized under PCM after they were isolated from these bacteria (Figure 2A). TEM showed that sGVs had a uniform cylindrical shape (Figure 2B). Figure 2C shows the FITC-labeled iRGD or FITC-labeled control peptide was successfully conjugated to the surface of GVs, resulting in an absorption peak at 488 nm from FITC. Both the resulting iRGD-sGVs and Con-sGVs have relatively uniform particle size distribution, with 164.53±1.47 nm for sGVs (PDI: 0.12±0.01), 165.20±3.51 nm for iRGD-sGVs (PDI: 0.12±0.02) and 164.43±1.20

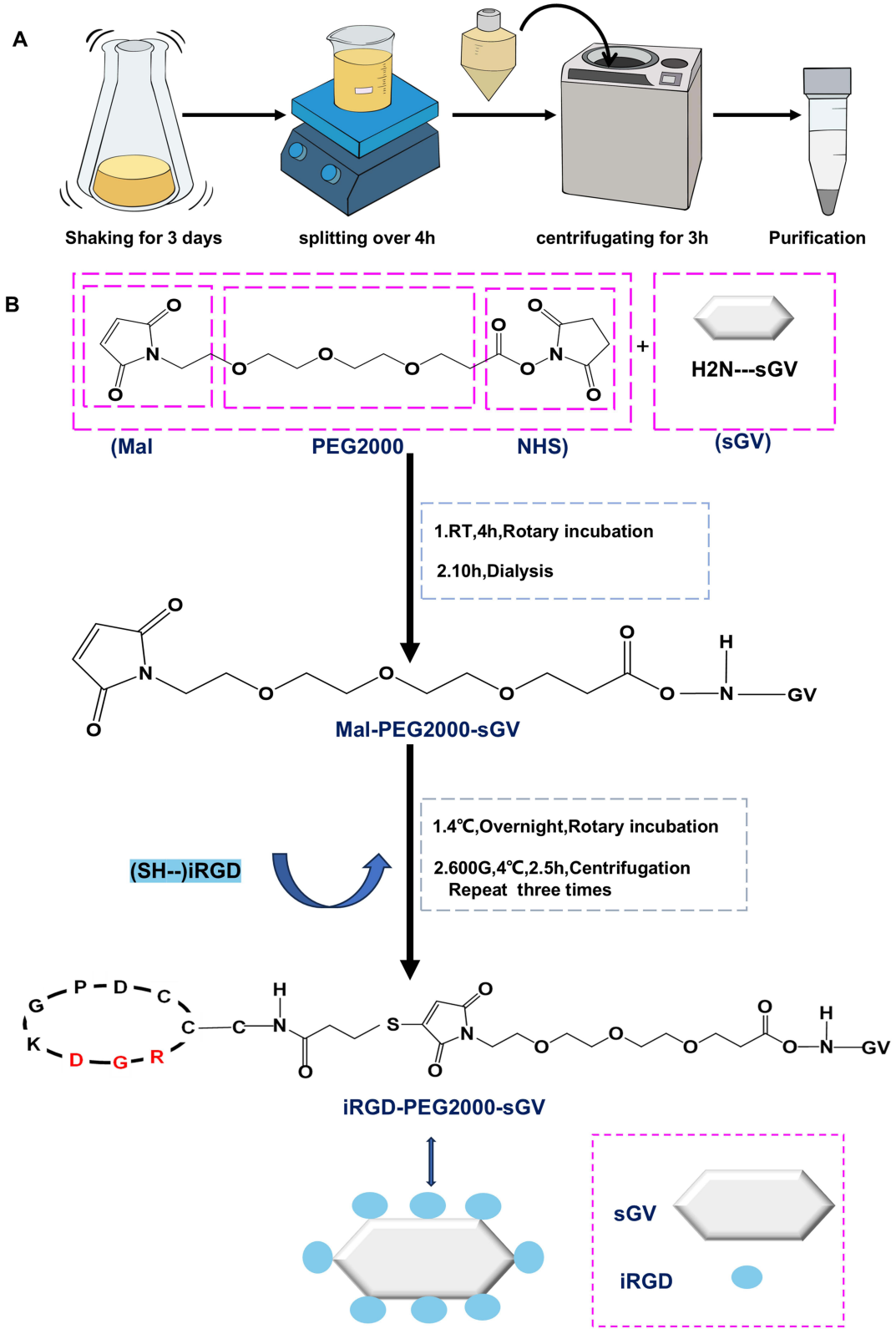

Figure 1 Preparation of sGVs, iRGD-sGVs and Con-sGVs. (**A**) Schematic diagram of separation and purification of sGVs. (**B**) Schematic diagram of fabrication of iRGD-sGVs.

nm for Con-sGVs (PDI: 0.12±0.01), respectively (Figure 2D-F). The zeta potential of sGVs, iRGD-sGVs and Con-sGVs were −21.3±0.6mV, −13.6±0.9mV and −11.5±0.5mV, respectively (Figure 2G). These results indicated that iRGD-sGVs and Con-sGVs had no significant difference in particle size and zeta potential (Figure 2H).

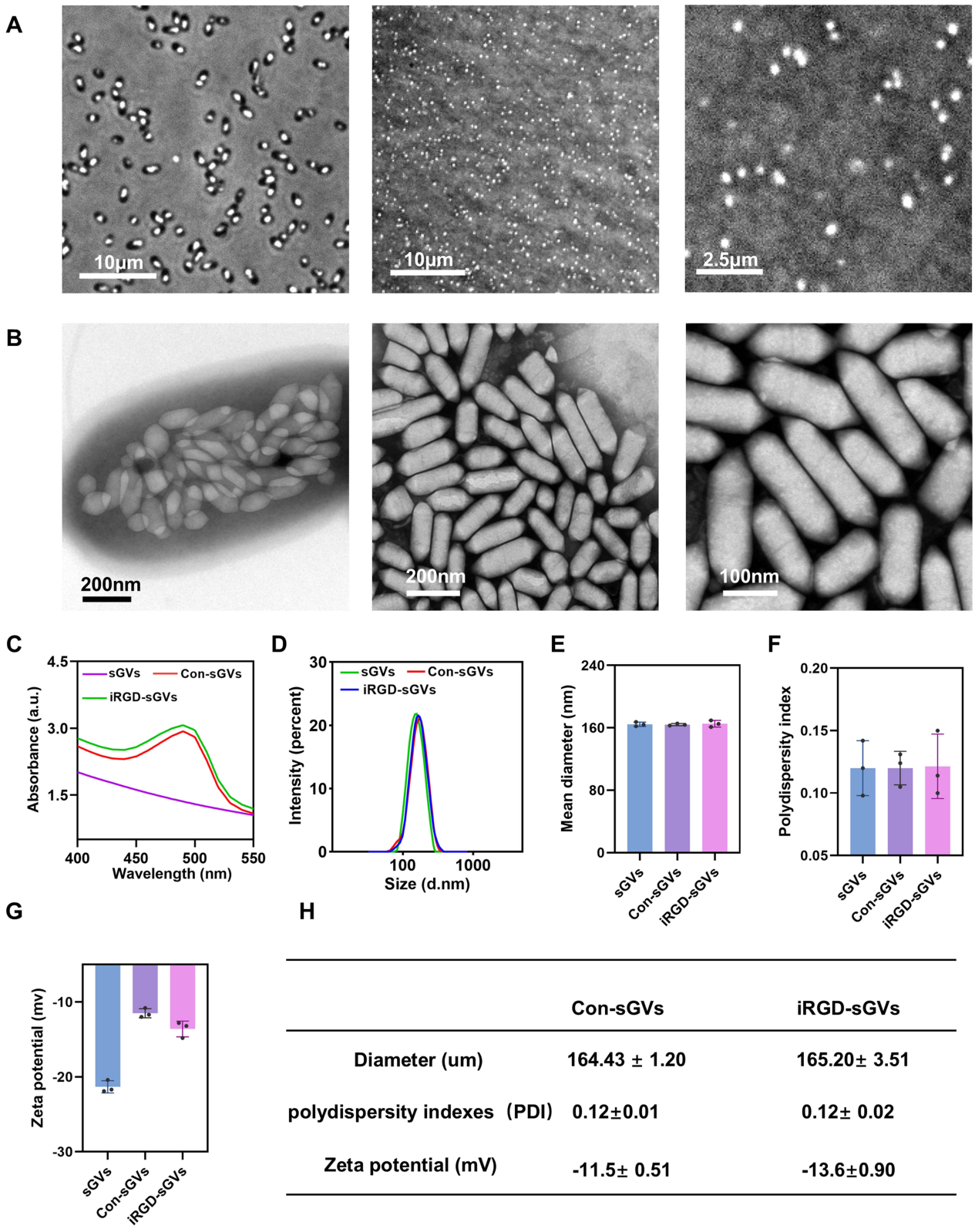

	Con-sGVs	iRGD-sGVs
Diameter (um)	164.43 ± 1.20	165.20± 3.51
polydispersity indexes (PDI)	0.12±0.01	0.12± 0.02
Zeta potential (mV)	-11.5± 0.51	-13.6±0.90

Figure 2 Characterization of sGVs, Con-sGVs and iRGD-sGVs. (**A**) PCM images of *Serratia* bacteria and sGVs. (**B**) TEM images of *Serratia* bacteria and sGVs. (**C**) Absorbance spectra of sGVs, Con-sGVs and iRGD-sGVs. (**D**) Size distribution of sGVs, Con-sGVs and iRGD-sGVs. (**E**) The mean diameters of sGVs, Con-sGVs and iRGD-sGVs. (**F**) PDI of sGVs, Con-sGVs and iRGD-sGVs. (**G**) Zeta potential of sGVs, Con-sGVs and iRGD-sGVs. (**H**) Comparison of diameters, PDI and zeta potential of Con-sGVs and iRGD-sGVs.

https://doi.org/10.2147/IJN.S494151

In vitro Imaging Capability of sGVs and Stability of iRGD-sGVs

Firstly, we compared sGVs with traditional chemically synthesized phospholipid nanobubbles in vitro. As shown in Figure S1A, the contrast signals of sGVs increased along with the increase of sGVs concentration. A comparable signal enhancement similar with traditional nanobubbles can achieve when the concentration of sGVs at OD500=3.0. Importantly, Figure S1B demonstrated that sGVs exhibited superior mechanical index tolerance, making them keep stability under higher ultrasound energy. These findings highlight the significant potential of sGVs in ultrasound imaging. To further evaluate the acoustic contrast imaging performance of iRGD-sGVs, different concentrations of iRGD-sGVs and Con-sGVs from OD_{500} =1.0 to 2.5 were imaged at the contrast mode. Figure 3A clearly showed that iRGD-sGVs and Con-sGVs exhibited significantly enhanced contrast signals. Moreover, the higher the concentrations of iRGD-sGVs and Con-sGVs were, the stronger contrast signals of these probe sGVs would be. The quantitative analysis of the average signal intensity revealed that Con-sGVs and iRGD-sGVs had comparable contrast signals at the same concentrations (Figure 3B). Con-sGVs and iRGD-sGVs maintained a high in vitro imaging signal (Figure 3C) at OD_{500}= 2.5 during 10 days, and no significant concentration changes were detected, indicating both Con-sGVs and iRGD-sGVs have good stability (Figure 3D). Figure 3E and F show that the particle size remained basically stable during 20 days, and increased slightly at the 20th day, where a few agglomerations may be present. The relative stability of the zeta potential in Figure 3G also indicated the stability of the GVs despite slight changes in the later period.

In vitro Cell Targeting Studies

Flow cytometry assay showed that FITC-iRGD peptide but not the control peptide could efficiently bind with bEnd.3 cells and K7M2 cells. Notably, the binding efficiency of FITC-iRGD was significantly reduced after pre-blocking with iRGD peptides (Figure 4A). On average, 98.9% of K7M2 cells and 99.4% of bEnd.3 cells exposed to FITC-iRGD exhibited significant increases in fluorescence, compared to less than 4% of bEnd.3 cells and 27% of K7M2 cells exposed to control peptide (Figure 4B and C).

Meanwhile, the capability of iRGD-sGVs binding to bEnd.3 cells was detected by incubating iRGD-sGVs with bEnd.3 cells monolayer in a plate. Figure 4D shows a number of iRGD-sGVs were attached to bEnd.3 cells. By contrast, few non-targeted Con-sGVs were bound to these cells. As expected, hardly iRGD-sGVs were observed on bEnd.3 cells which were pre-incubated with free iRGD peptide (Figure 4D). Quantitative analysis showed that the number of iRGD-sGVs adhering to cells was significantly reduced by 8 times due to the blocking by free iRGD peptide (Figure 4E). Similar results were found on K7M2 cells (Figure 4D–F), indicating that iRGD-sGVs not only could bind with tumor vascular endothelial cells, but also with K7M2 osteosarcoma.

In vivo Tumor Imaging Performance of iRGD-sGVs

Next, we further evaluated the imaging performance of iRGD-sGVs in tumor-bearing mice. Con-sGVs and iRGD-sGVs were intravenously administered in random order. Figure 5A shows the schematic diagram of ultrasound molecular imaging of tumor-bearing mice. From Figure 5B, we can clearly see that there was no significant difference in peak signal intensity between Con-sGVs and iRGD-sGVs in K7M2 tumors (124.16 ± 21.29 a.u. for Con-sGVs, 123.35 ± 7.82 a.u. for iRGD-sGVs). However, along with the time, the signal intensity of the tumors received with iRGD-sGVs was significantly higher than that of tumors received with Con-sGVs (Figure 5B–D), achieving 121.33 ± 7.33 a.u. for iRGD-sGVs after 3 min. By contrast, the signal intensity of Con-sGVs significantly dropped to 79.92 ± 8.40 a. u at the same time point. Figure 5B–D clearly showed the slower decay curve of iRGD-sGVs group in comparison to Con-sGVs. The contrast signals of iRGD-sGVs were 2.13, 3.36 and 3.52-fold stronger than those of Con-sGVs at 5, 10 and 15 min after injection, confirming that iRGD-sGVs had excellent ultrasound molecular imaging performance in tumor-bearing mice.

Tumor Immunofluorescence Staining

To further validate the ultrasound molecular signals from iRGD-sGVs in the tumor, the tumors were harvested and the expression of $a_v\beta_3$ integrin was subsequently analyzed by immunofluorescence assay. The results showed co-localization of $a_v\beta_3$ with CD31,

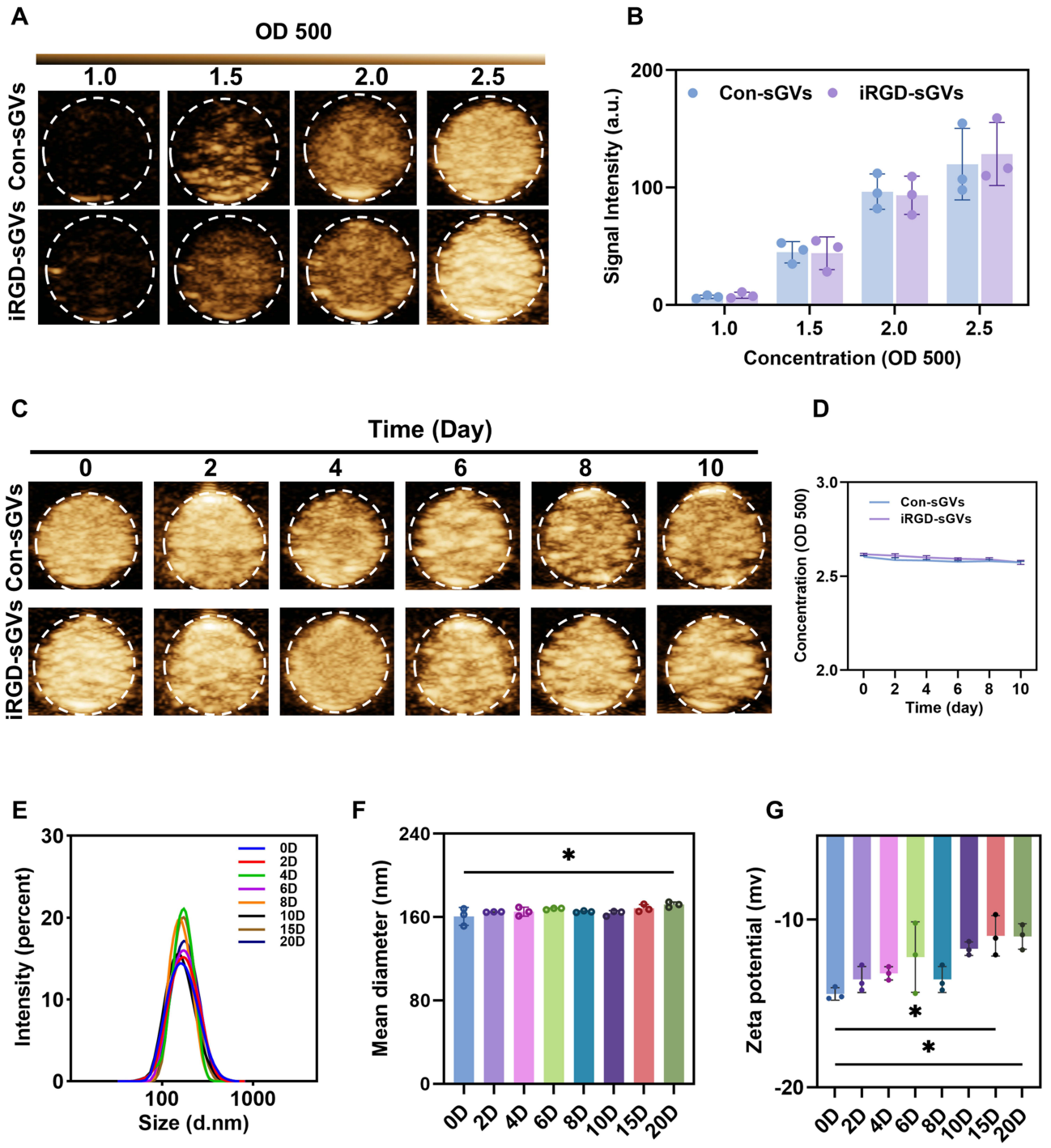

Figure 3 In vitro imaging ability and stability in the PBS of iRGD-sGVs and Con-sGVs. (**A**) The representative ultrasound contrast images of Con-sGVs and iRGD-sGVs at different concentrations. (**B**) The quantitative analysis of Con-sGVs and iRGD-sGVs (n=3). (**C**) The representative ultrasound contrast images of Con-sGVs and iRGD-sGVs in 10 days. (**D**)Stability testing of Con-sGVs and iRGD-sGVs at OD_{500} = 2.5. (**E**) Particle size of iRGD-sGVs over 20-day period. (**F**) The mean diameters of iRGD-sGVs over 20-day period. (**G**) Zeta potential of iRGD-sGVs over 20-day period. *P < 0.05.

confirming the presence of $a_v\beta_3$ integrin on angiogenic endothelial cells within the K7M2 tumors used in this study (Figure 5E). Notably, we also observed the green fluorescence signal of anti-$a_v\beta_3$ antibody on K7M2 tumor cells, apart from vascular endothelial cells. The results indicated $a_v\beta_3$ integrin plays an important role in both angiogenesis and cell proliferation of osteosarcoma. More importantly, the high-level expression of $a_v\beta_3$ integrin and effective binding property of iRGD to $a_v\beta_3$

https://doi.org/10.2147/IJN.S494151

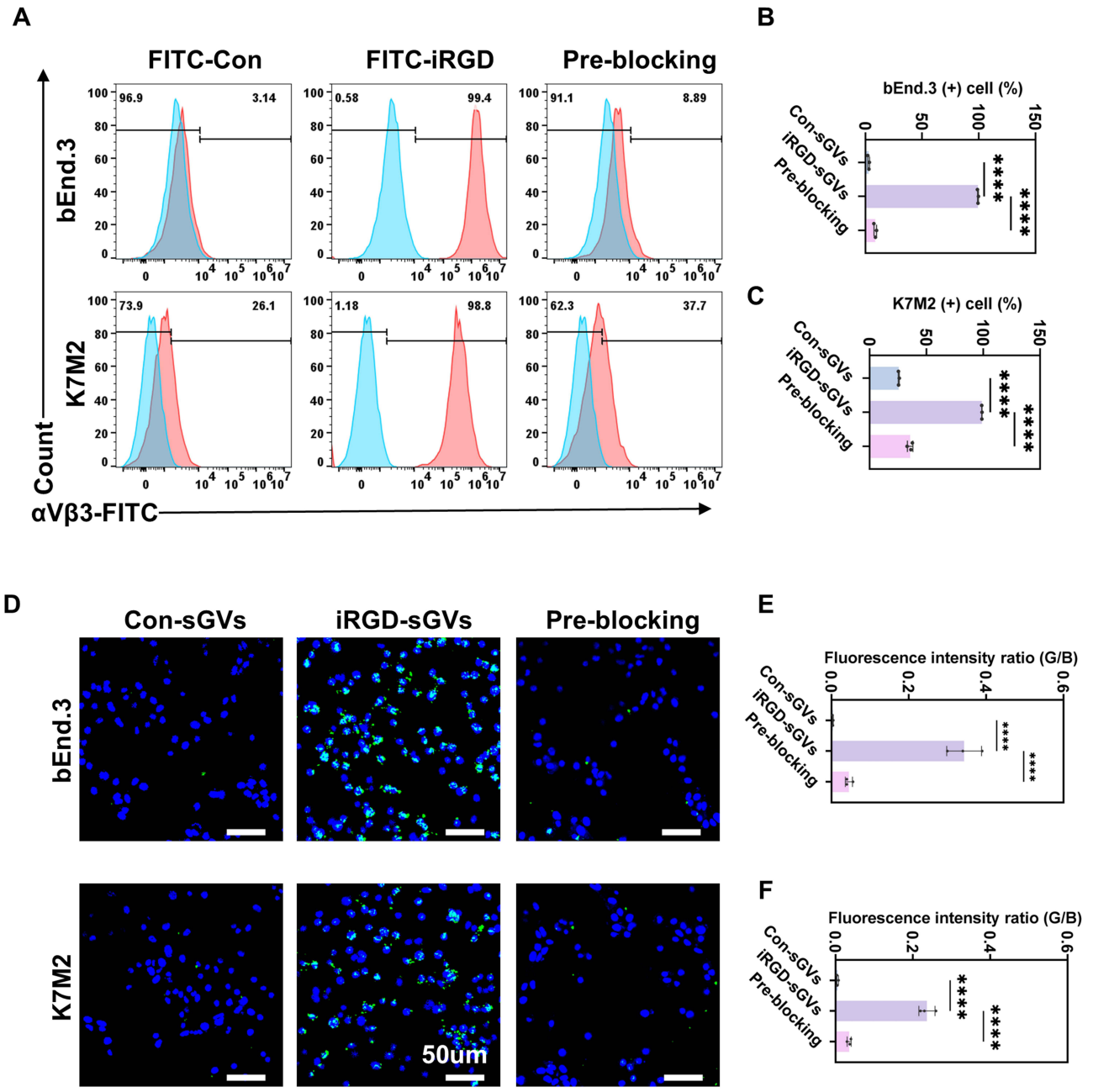

Figure 4 In vitro cell targeting studies. (**A**) Flow cytometry assay of Bend.3 cells and K7M2 cells incubated with FITC-Con, FITC-iRGD or free iRGD + FITC-iRGD, respectively. (**B**) Quantitative analysis of bEnd.3 cells binding with FITC-Con or FITC-iRGD. (**C**) Quantitative analysis of K7M2 cells binding with FITC-Con or FITC-iRGD. (**D**) Representative fluorescent microscope images of bEnd3 cells and K7M2 cells incubated with FITC-Con-sGVs, FITC-iRGD-sGVs or free iRGD + FITC-iRGD-sGVs. Green stands for FITC, and blue for cell nuclei stained with DAPI. Scale bar: 50 μm. (**E**) and (**F**) Quantitative analysis of fluorescence intensities from (**D**). **** for $P < 0.0001$.

integrin makes iRGD especially suitable for the ligand of targeted probes, providing an innovative tool for the early diagnosis of osteosarcoma.

Biosafety Assay

The hemolysis test results are shown in Figure 6A, revealing that there was no hemolysis or agglutination of erythrocytes at different concentrations of iRGD-sGVs. By contrast, obvious hemolysis was observed in H_2O-treated sample as a positive control. Besides, the supernatants of samples treated with iRGD-sGVs were transparent and colorless after

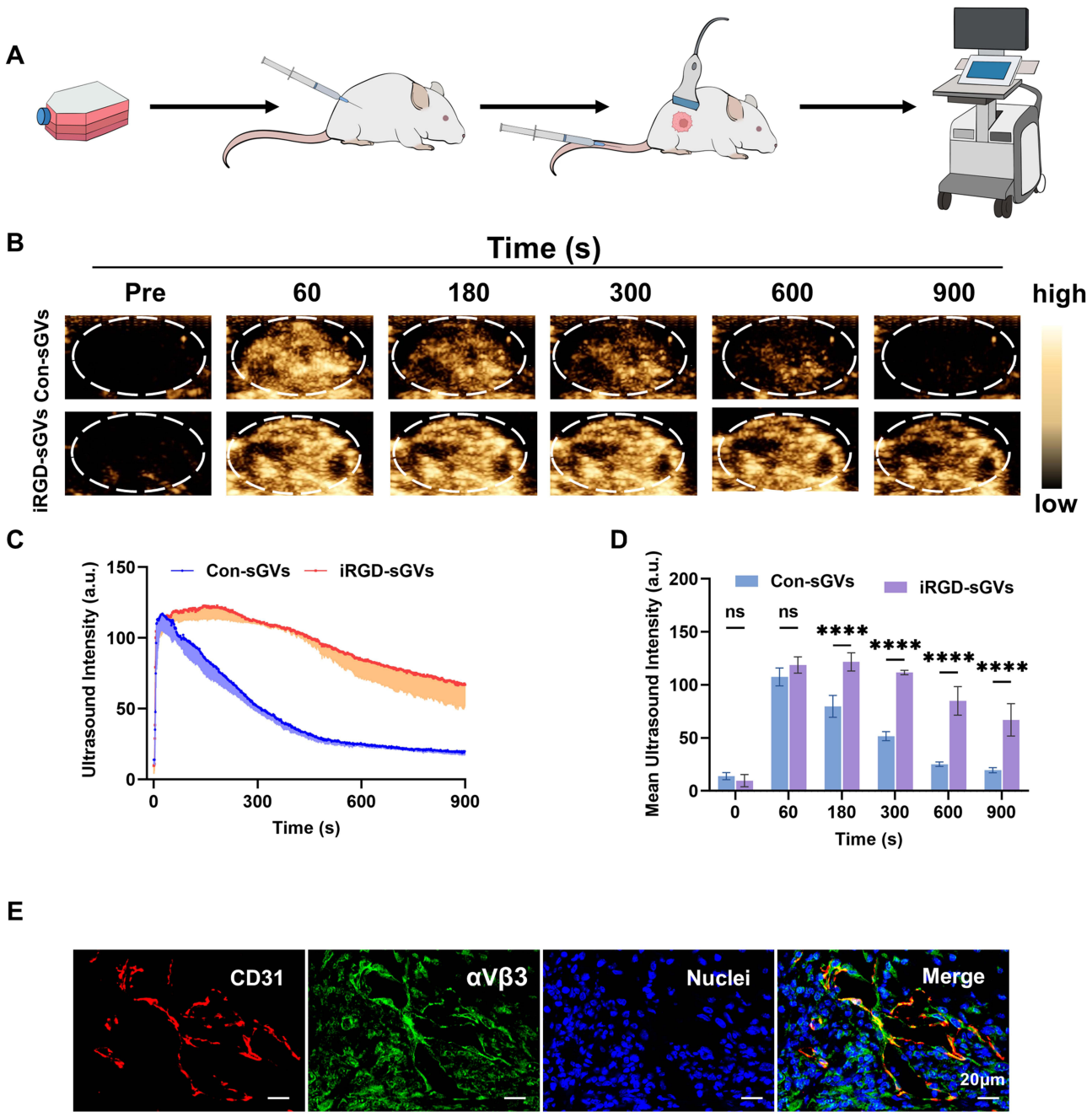

Figure 5 In vivo ultrasound molecular imaging of tumors. (**A**)The schematic diagram of ultrasound molecular imaging of tumor-bearing mice. (**B**)Nonlinear contrast images of Con-sGVs or iRGD-sGVs at different time after intravenous injection. (**C**) Time–intensity curves of Con-sGVs and iRGD-sGVs after intravenous injection. (**D**) The contrast signal intensities of tumors received with Con-sGVs and iRGD-sGVs at 1, 3, 5, 10 and 15 min. (**E**) Blood vessel, $a_v\beta_3$ and DAPI in K7M2 tumors were stained with immunofluorescence. ns indicates no statistical difference, **** for $P < 0.0001$.

centrifugation, just like PBS-treated sample. Moreover, there was no significant difference between PBS and iRGD-sGVs, suggesting iRGD-sGVs did not damage to the red cells. Furthermore, different concentrations of iRGD-sGVs were incubated with K7M2 and bEnd.3 cells, and CCK8 assays showed that iRGD-sGVs did not produce significant cytotoxicity to K7M2 and bEnd.3 cells (Figure 6B). Also, the cell safety of sGVs was assessed with Calcein-AM and PI staining, followed by observation with confocal microscopy. As shown in Figure S2, K7M2 cells and bEnd.3 cells showed bright green fluorescence, indicating that sGVs had no obvious cytotoxicity to these cells. In addition, the in vivo biosafety was analyzed through detecting blood samples of healthy mice injected with iRGD-sGVs or Con-sGVs. The

https://doi.org/10.2147/IJN.S494151

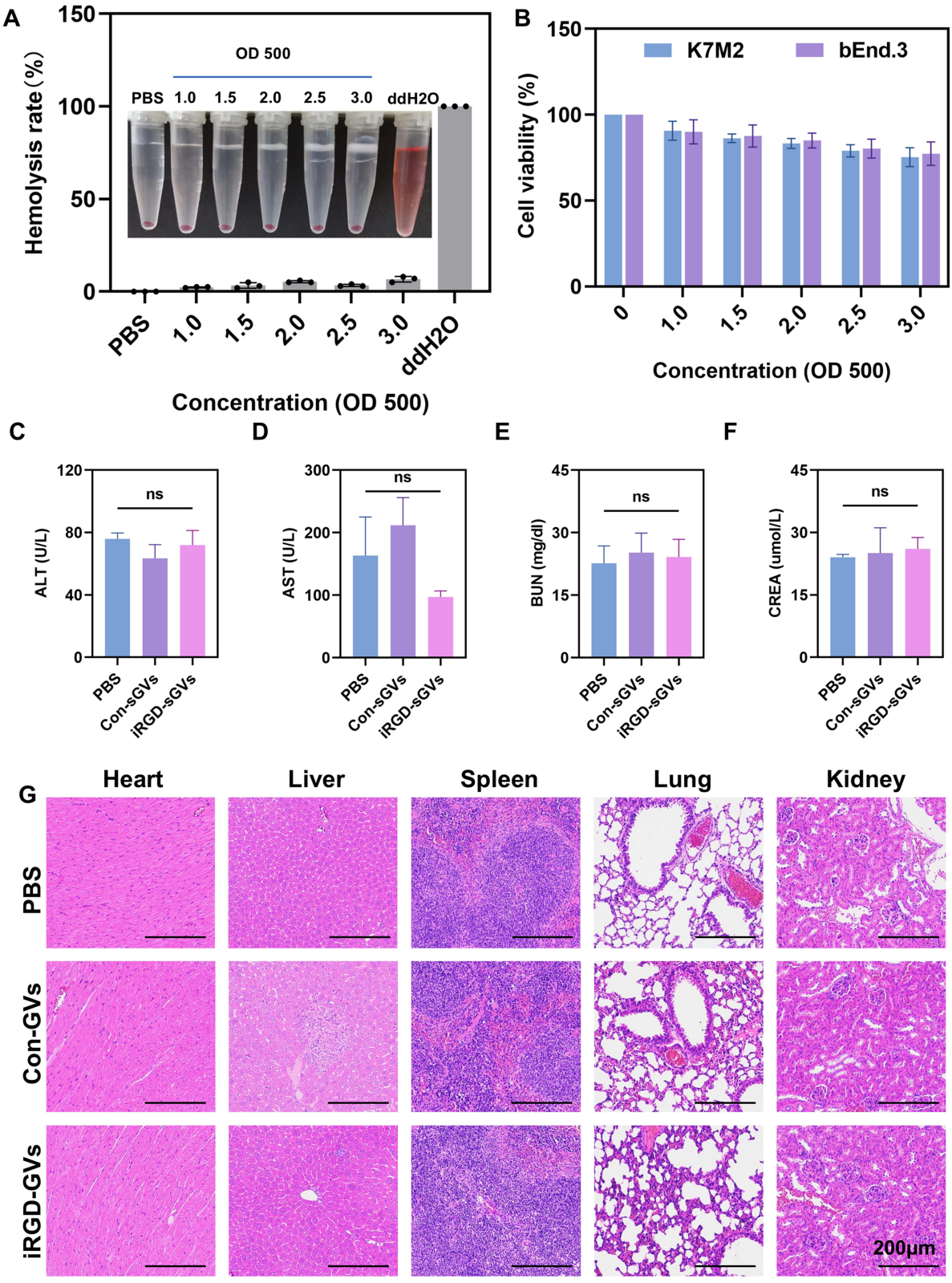

Figure 6 Biosafety analysis. (**A**) Hemolysis assay for iRGD-sGVs at OD_{500} = 1.0, 1.5, 2.0,2.5 or 3.0, using double-distilled water (ddH2O) as a positive control and PBS as a negative control, n = 3. (**B**) Cell viability of bEnd.3 cells and K7M2 cells after treatment with iRGD-sGVs at OD_{500} = 1.0, 1.5, 2.0,2.5 or 3.0 for 6 h, n = 3. (**C–F**) The level of liver function (ALT, AST), renal function (BUN, CREA) after 7 days post-injection of PBS control, Con-sGVs or iRGD-sGVs (n = 3). (**G**) H&E staining of major organs (heart, liver, spleen, lung and kidney) in mice received with Con-sGVs, iRGD-sGVs or PBS at OD_{500} 3.0. The scale is 200 μm. ns indicates no statistical difference.

https://doi.org/10.2147/IJN.S494151

data revealed that the blood biochemical indexes such as liver and kidney function had no obvious abnormal changes (Figure 6C-F). H&E staining analysis did not find pathological damage to the heart, liver, spleen, lungs, and kidneys, similar with PBS-treated controls (Figure 6G). These results suggest that iRGD-sGVs had excellent biosafety.

Discussion

Osteosarcoma is one of the most common malignant tumors of the bone. It is highly invasive and easy to spread and metastasize through blood in the early stage of tumors, producing a serious impact on patients.[23,24] The application of molecular imaging has shown great potential in early-stage diagnosis of tumors.[13] The complex interstitial components of osteosarcoma make these tumor cells more easily escape immune, produce chemotherapy resistance and metastasis.[25–27] Recent studies have shown that the transmembrane protein integrin $\alpha_v\beta_3$ is not only highly expressed in tumor blood vessels, but also significantly expressed in osteosarcoma cells.[28] This finding highlights the role of integrins in osteosarcoma and provides an ideal imaging and therapeutic target. In this study, we selected it as the imaging target and fabricated iRGD-sGVs acoustic probe for the early-stage diagnosis of osteosarcoma.

As the ligand of $\alpha_v\beta_3$ receptor, the iRGD peptide contains an RGD sequence targeting to $\alpha_v\beta_3$ integrin, a C-terminal rule (CendR) motif, and a protease recognition site.[29] The RGD targeting recognition sequence can specifically bind to integrin $\alpha_v\beta_3$, which are highly expressed on the surface of tumor vascular endothelial cells and tumor cells.[20] Takashi Temma's group successfully imaged integrin $\alpha_v\beta_3$ in cancer using radioiodine-labeled bicyclic RGD peptides.[30] Wang et al maintained its targeting and penetrating biological activity by modifying iRGD on nanopolymers, so that iRGD-modified nanoparticles have excellent tumor cell uptake and tumor penetration.[31] These results suggest that iRGD has important potential application value in cancer imaging and treatment.

Recently, biosynthetic nanobubbles have attracted much attention as ultrasound contrast agents due to their high stability, low toxicity, easy post-modification, and genetically engineering characteristics. The protein shell-inflated GVs from *Anabaena flos-aquae* and *Halobacterium sp. NRC-1* were firstly reported by Shapiro et al, providing stable contrast-enhanced acoustic signals.[32] Our group has successfully demonstrated the biosynthetic hGVs from *Halobacterium sp. NRC-1* can be detected by clinical ultrasound diagnostic equipment.[10,13] In our recent study, we extracted and purified another biosynthetic nanobubbles from *Serratia*.39006.[33] Compared with hGVs from *Halobacterium sp. NRC-1*, sGVs from *Serratia*.39006 have smaller particle size (about 160 nm), negative charge and rod shape, endowing them with stronger tumor permeability capability.[18] On the other hand, it is reasonable about the imaging mechanism of biologically synthesized nano-scale GVs and the contrast-enhanced acoustic signals in the tumor. In fact, GVs are made up of 2-nm thick protein shells. Gases or air from liquid water are encapsulated in the shells when these GVs grow up in the bacteria.[34] The presence of gases endows these GVs with the ability to scatter acoustic waves. Also, the soft protein shells make it possible produce rich harmonic signals when GVs are excited by ultrasound waves.[35,36] As for the reasons why bacterial derived GVs can target tumor tissue and produce contrast-enhanced acoustic signals, it can mainly attribute to the nanoscale size of GVs. Compared with the particle size of microbubbles (1–5 μm), GVs have only 100–200 nm particle size. Due to the presence of enhanced permeability and retention (EPR) effect in the tumor, nanoscale GVs can penetrate tumor blood vessels and be enriched in the tumor tissue, producing contrast-enhanced acoustic signals.

In this study, we used the maleimide-mercapto conjugation method, rather than the chemical method of biotin-streptavidin linkage, to design iRGD-targeted sGVs (iRGD-sGVs), overcoming the limitation of immunogenicity from streptavidin.[37] In contrast, the maleimide-thiol conjugation reaction provides a highly specific and efficient method for conjugating the targeting ligands to the nanobubble surface.[38] The covalent bonds formed by this method exhibited fair stability in vitro and in vivo, which is crucial for maintaining the integrity and function of the nanobubbles during storage and administration. Moreover, several studies have shown that PEG modification can reduce the immunogenicity of biomaterials.[39] In our study, we used the MAL-PEG2000-NHS to make full use of the advantages of PEG modification, not only improving the biocompatibility of sGVs, but also prolonging their circulation time in vivo. All of these features make iRGD-sGVs successfully achieve ultrasound molecular imaging in osteosarcoma-bearing mice.

Nevertheless, our research still has some limitations. Firstly, gas vesicles with a particle size of 160 nm have individual differences in the imaging of osteosarcoma. For tumors with poor blood supply, the imaging effect is poor, and its imaging parameters need to be further optimized. Secondly, the utilization of a subcutaneous tumor model also

limits its translation applicability to clinical conditions. In view of the absorption and scattering characteristics of bone tissue, the ultrasonic signals are hindered in the penetration process of sound wave, so the signal intensity is not enough to accurately reflect the location and size of the tumor. The clinical validation data of biosynthetic targeted contrast agents in ultrasound imaging of osteosarcoma are relatively limited, so their effects in practical clinical practice still need to be further verified. These limitations need to be fully considered in future research, and we will continue to work to solve these problems to improve the accuracy and reliability of imaging technology and provide stronger support for clinical treatment.

Conclusion

In conclusion, we developed iRGD-modified nanoscale imaging agents (iRGD-sGVs), holding great potential for improving the precision, sensitivity, and early diagnosis of osteosarcoma. By taking advantages of biologically synthesized gas vesicles and the specificity of the iRGD peptide, our study paves the way to realizing more effective and personalized strategies in cancer imaging and treatment. The future research would further focus on optimizing and validating this innovative imaging approach for clinical translation and potential integration into routine oncology practice.

Data Sharing Statement

All the data and associated raw data from the manuscript are available upon reasonable request from the authors.

Acknowledgments

The authors gratefully acknowledge the support of the National Key R&D Program of China (2020YFA0908800), the National Natural Science Foundation of China (32171365), Guangdong Innovation Platform of Translational Research for Cerebrovascular Diseases, the Shenzhen Medical Research Fund (grant no. D2301012, B2402006), the Shenzhen Institute of Synthetic Biology Scientific Research Program (grant no. JCHZ20210002), Shenzhen Second People's Hospital Clinical Research Fund of Guangdong Province High-level Hospital Construction Project (Grant No.20213357014), Medical-Engineering Interdisciplinary Research Foundation of Shenzhen University (Grant No.2023YG032).

Disclosure

The authors report no conflicts of interest in this work.

References

1. Evdokimova V, Gassmann H, Radvanyi L, Burdach SEG. Current State of Immunotherapy and Mechanisms of Immune Evasion in Ewing Sarcoma and Osteosarcoma. *Cancers*. 2023;15.
2. Czarnecka AM, Synoradzki K, Firlej W, et al. Molecular Biology of Osteosarcoma. *Cancers*. 2020;12:2130. doi:10.3390/cancers12082130
3. Zheng HR, Kruse DE, Stephens DN. A novel sensitive targeted imaging technique for ultrasonic molecular imaging. *IEEE Ultrasonics Symposium*. New York, NY 2007; 957–960.
4. Xiong XY, Zhao FL, Shi MR, Yang H, Liu YY. Polymeric Microbubbles for Ultrasonic Molecular Imaging and Targeted Therapeutics. *J Biomater Sci-Polym Ed*. 2011;22:417–428. doi:10.1163/092050610X540440
5. Kosareva A, Abou-Elkacem L, Chowdhury S, Lindner JR, Kaufmann BA. Seeing the Invisible-Ultrasound Molecular Imaging. *Ultrasound Med Biol*. 2020;46:479–497. doi:10.1016/j.ultrasmedbio.2019.11.007
6. Zhong JL, Huang LC, Su MT, et al. Ultrasound Microvessel Visualization in Cervical Cancer: association Between Novel Ultrasound Techniques and Histologic Microvessel Densities. *Ultrasound Med Biol*. 2023;49:2537–2547. doi:10.1016/j.ultrasmedbio.2023.08.017
7. Petitprez F, Vano YA, Becht E, et al. Transcriptomic analysis of the tumor microenvironment to guide prognosis and immunotherapies. *Cancer Immunol Immunother*. 2018;67:981–988. doi:10.1007/s00262-017-2058-z
8. Liu J, Dang H, Wang XW. The significance of intertumor and intratumor heterogeneity in liver cancer. *Exp Mol Med*. 2018;50:e416. doi:10.1038/emm.2017.165
9. Schmitz G. Ultrasonic imaging of molecular targets. *Basic Research in Cardiology*. 2008;103:174–181. doi:10.1007/s00395-008-0709-0
10. Zhao P, Zhao S, Zhang JQ, Lai ML, Sun LT, Yan F. Molecular Imaging of Steroid-Induced Osteonecrosis of the Femoral Head through iRGD-Targeted Microbubbles. *Pharmaceutics*. 2022;14:1898. doi:10.3390/pharmaceutics14091898
11. Deshpande N, Pysz MA, Willmann JK. Molecular ultrasound assessment of tumor angiogenesis. *Angiogenesis*. 2010;13:175–188. doi:10.1007/s10456-010-9175-z

12. Liu XS, Lin P, Perrett I, et al. Tumor-penetrating peptide enhances transcytosis of silicasome-based chemotherapy for pancreatic cancer. *J Clin Investig*. 2017;127:2007–2018. doi:10.1172/JCI92284
13. Hao Y, Li Z, Luo J, Li L, Yan F. Ultrasound Molecular Imaging of Epithelial Mesenchymal Transition for Evaluating Tumor Metastatic Potential via Targeted Biosynthetic Gas Vesicles. *Small*. 2023;19:e2207940. doi:10.1002/smll.202207940
14. Zheng YW, Liu MY, Jiang LX. Progress of photoacoustic imaging combined with targeted photoacoustic contrast agents in tumor molecular imaging. *Front Chem*. 2022;10.
15. He YN, Zhou MJ, Li SS, Gong ZL, Yan F, Liu HM. Ultrasound Molecular Imaging of Neovascularization for Evaluation of Endometrial Receptivity Using Magnetic iRGD-Modified Lipid-Polymer Hybrid Microbubbles. *Int j Nanomed*. 2022;17:5869–5881. doi:10.2147/IJN.S359065
16. Wei MJ, Lai ML, Zhang JQ, Pei XQ, Yan F. Biosynthetic Gas Vesicles from Halobacteria NRC-1: a Potential Ultrasound Contrast Agent for Tumor Imaging. *Pharmaceutics*. 2022;14:1198. doi:10.3390/pharmaceutics14061198
17. Lakshmanan A, Lu GJ, Farhadi A, et al. Preparation of biogenic gas vesicle nanostructures for use as contrast agents for ultrasound and MRI. *Nature Protocols*. 2017;12:2050–2080. doi:10.1038/nprot.2017.081
18. Li P, Wang D, Hu J, Yang X. The role of imaging in targeted delivery of nanomedicine for cancer therapy. *Adv Drug Deliv Rev*. 2022;189:114447. doi:10.1016/j.addr.2022.114447
19. Kang H, Rho S, Stiles WR, et al. Size-Dependent EPR Effect of Polymeric Nanoparticles on Tumor Targeting. *Adv Healthc Mater*. 2020;9: e1901223. doi:10.1002/adhm.201901223
20. Qian J, Zhou S, Lin P, et al. Recent advances in the tumor-penetrating peptide internalizing RGD for cancer treatment and diagnosis. *Drug Dev. Res*. 2023;84:654–670. doi:10.1002/ddr.22056
21. Saifi MA, Sathish G, Bazaz MR, Godugu C. Exploration of tumor penetrating peptide iRGD as a potential strategy to enhance tumor penetration of cancer nanotherapeutics. *Biochimica Et Biophysica Acta-Reviews on Can*. 2023;1878:188895. doi:10.1016/j.bbcan.2023.188895
22. Li DY, Li JR, Wang SW, Teng W, Wang QM. Combined Self-Assembled iRGD Polymersomes for Effective Targeted siRNA Anti-Tumor Therapy. *Int j Nanomed*. 2022;17:5679–5696. doi:10.2147/IJN.S383862
23. Tian HL, Cao JJ, Li BW, et al. Managing the immune microenvironment of osteosarcoma: the outlook for osteosarcoma treatment. *Bone Res*. 2023;11.
24. Belayneh R, Fourman MS, Bhogal S, Weiss KR. Update on Osteosarcoma. *Current Oncology Reports*. 2021;23. doi:10.1007/s11912-021-01053-7
25. Yuan P, Min Y, Zhao Z. Multifunctional nanoparticles for the treatment and diagnosis of osteosarcoma. *Biomater Adv*. 2023;151:213466. doi:10.1016/j.bioadv.2023.213466
26. Smrke A, Anderson PM, Gulia A, Gennatas S, Huang PH, Jones RL. Future Directions in the Treatment of Osteosarcoma. *Cells*. 2021;10:172. doi:10.3390/cells10010172
27. Tsagozis P, Gonzalez-Molina J, Georgoudaki AM, et al. Sarcoma Tumor Microenvironment. *Adv Exp Med Biol*. 2020;1296:319–348.
28. Tome Y, Kimura H, Sugimoto N, et al. The disintegrin echistatin in combination with doxorubicin targets high-metastatic human osteosarcoma overexpressing αvβ3 integrin in chick embryo and nude mouse models. *Oncotarget*. 2016;7:87031–87036. doi:10.18632/oncotarget.13497
29. Kadonosono T, Yamano A, Goto T, et al. Cell penetrating peptides improve tumor delivery of cargos through neuropilin-1-dependent extravasation. *J Control Release*. 2015;201:14–21. doi:10.1016/j.jconrel.2015.01.011
30. Kondo N, Wakamori K, Hirata M, Temma T. Radioiodinated bicyclic RGD peptide for imaging integrin α(v)β(3) in cancers. *Biochem Biophys Res Commun*. 2020;528:168–173. doi:10.1016/j.bbrc.2020.05.106
31. Wang Y, Xie Y, Li J, et al. Tumor-Penetrating Nanoparticles for Enhanced Anticancer Activity of Combined Photodynamic and Hypoxia-Activated Therapy. *ACS Nano*. 2017;11:2227–2238. doi:10.1021/acsnano.6b08731
32. Shapiro MG, Ramirez RM, Sperling LJ, et al. Genetically encoded reporters for hyperpolarized xenon magnetic resonance imaging. *Nature Chem*. 2014;6:630–635. doi:10.1038/nchem.1934
33. Liu T, Wang J, Liu C, Wang Y, Li Z, Yan F. Characterization and Comparison of Contrast Imaging Properties of Naturally Isolated and Heterologously Expressed Gas Vesicles. *Pharmaceuticals (Basel)*. 2024;17:755. doi:10.3390/ph17060755
34. Walsby AE. Gas vesicles. *Microbiol Rev*. 1994;58:94–144. doi:10.1128/mr.58.1.94-144.1994
35. Maresca D, Payen T, Lee-Gosselin A, et al. Acoustic biomolecules enhance hemodynamic functional ultrasound imaging of neural activity. *Neuroimage*. 2020;209:116467. doi:10.1016/j.neuroimage.2019.116467
36. Shapiro MG, Goodwill PW, Neogy A, et al. Biogenic gas nanostructures as ultrasonic molecular reporters. *Nat Nanotechnol*. 2014;9:311–316. doi:10.1038/nnano.2014.32
37. Meyer DL, Schultz J, Lin Y, et al. Reduced antibody response to streptavidin through site-directed mutagenesis. *Protein Sci*. 2001;10:491–503. doi:10.1110/ps.19901
38. Choi KY, Min KH, Yoon HY, et al. PEGylation of hyaluronic acid nanoparticles improves tumor targetability in vivo. *Biomaterials*. 2011;32:1880–1889. doi:10.1016/j.biomaterials.2010.11.010
39. Wang G, Song L, Hou X, et al. Surface-modified GVs as nanosized contrast agents for molecular ultrasound imaging of tumor. *Biomaterials*. 2020;236:119803. doi:10.1016/j.biomaterials.2020.119803